Direct numerical modeling of time-reversal acoustic subwavelength focusing

Ming Zhao, Yann Capdeville, Huai Zhang

Direct numerical modeling of time-reversal acoustic subwavelength focusing

MING ZHAO[a,b,c,*], YANN CAPDEVILLE[b], HUAI ZHANG[a,c]

[a] *Laboratory of Computational Geodynamics, Chinese Academy of Sciences, Beijing, China*
[b] *Laboratoire de Planétologie et Géodynamique de Nantes, CNRS, Université de Nantes, France*
[c] *University of Chinese Academy of Sciences, Beijing 100049, China*

Abstract

Focusing waves back to their original source position is possible both experimentally and numerically thanks to time reversal mirrors (TRM). For a TRM placed in the source far-field, the focusing spot of the reversed wavefield is subject to the diffraction limit and can't be smaller than half the minimum wavelength, even for a very small source. Yet, numerous time reversal experiments in resonating media have shown subwavelength focusing. In this work, we show that it is possible to model these subwavelength focusing observations with simple physics, only the 2-D standard acoustic wave equation, and with specific fine scale heterogeneity. Our work is based on the spectral element method to solve the wave equation and to model time reversal experiments. Such a method makes it possible to propagate very long time series in complex and strongly discontinuous media with high accuracy. The acoustic wave equations are solved at the fine scale in media with one or more split rings of size much smaller than the wavelength. Such split rings produce a Helmholtz resonance effect as well as propagation band-gaps. We show that, in such media, even with a single split ring resonator, subwavelength focusing down to 1/13th of the minimum wavelength can be observed.

*Corresponding author
Email address: mingzhao@ucas.ac.cn (MING ZHAO)

1. Introduction

Waves created by a localized source diverge from their origin and time reversal methods have the ability to focus these waves back to their original source location using a time reversal mirror (TRM) regardless how complex the media are, provided that there is no attenuation. It is based on the theory of time reversal invariance and spatial reciprocity of the wave equations [1], provided that the attenuation can be neglected. It has been widely studied in the acoustic [2, 3, 4, 5], ultrasound acoustic [6, 7, 8], electromagnetic [9, 10] and elastic wave domains [11, 12]. In seismology, it has been used in seismic interferometry, earthquake source localization and reconstruction [13, 14], or in tomographic imaging [15].

The diffraction limit is a well known wave phenomenon which can be observed in many circumstances such as refocusing of light by optical lens [16, 17]. It states that any focusing and imaging resolution of acoustic, elastic or electromagnetic waves, has a resolution limit of $\lambda/2$, where λ is the wavelength. Indeed, wavefield spatial variations smaller than $\lambda/2$, such as evanescent waves in the near-field of a point source (see [1] page 72 for a precise definition of the source near-field), decrease very quickly from its origin and become negligible just a few wavelengths away. It can be shown that, for a TRM placed in the far-field of a source (that is, a few wavelengths away), regardless how spatially small the source is, the focusing spot at the source original location can never be smaller than roughly half of the wavefield wavelength [18]: this is the so-called diffraction limit. Nevertheless, one of the most astonishing observation about time reversal is the subwavelength focusing which, in some specific media, beats the diffraction limit [19]. Recent works, such as "superlens" designed by metamaterial with negative index of refraction to enhance the evenscant waves in the near field [20, 21, 22, 23], or "hypenlens" made of anisotropic metamaterial with hyperbolic dispersion relations to transfer the evanescent waves into propagating waves [24, 25], show subwavelength imaging capacity.

In homogeneous media, the spatial resolution of the time reversal focusing spot is limited not only by the diffraction limit, but also the aperture of the TRM. However, when the medium between the source and the TRM is heterogeneous and strongly scat-

tering, the focusing resolution will be enhanced significantly [26, 27], but not beyond the diffraction limit. Nevertheless, Mathias Fink and his group achieved the subwavelength focal spot by using an "acoustic sink" in the time reversal refocusing process, although an active time-reversed source must be used to recover the evanescent waves [28]. A more meaningful experiment designed by [29] showed focal spots far beyond the diffraction limit ($\lambda/13$) in the electromagnetic domain with TRM placed in the far field, and a random distribution of scatterers placed in the near field of the focusing point. Following this work, it has been shown that strongly coupled subwavelength Helmholtz resonators, for example, an array of soda cans, can be very efficient to focus waves to the subwavelength scale from the far field [30, 31]. The Helmholtz resonator has been reported to have negative effective bulk modulus, and can be used for the design of negative acoustic index metamaterials [32, 33]. These experiments promise a wide range of applications in various fields such as telecommunications [34], underwater communications [35, 36], optical imaging [37], sensing at higher frequencies [38, 39].

The numerous observations of time reversal subwavelength focusing mentioned above are intriguing, especially for the soda cans experiment. Recent results show the same sharp focusing spot but with soda cans arranged in a different way and without using time-reversal [40]. However, the authors of this later recent work conclude that no sub-diffraction-limited focusing is observed if the diffraction limit is defined with respect to the wavelength of the guided mode in the metamaterial medium rather than the wavelength of the bulk wave in air. A complete understanding of the processes involved is not trivial and is bounded by observation and experimental limitations such as the one linked to the dissipation loss of the media, which reduce the resonance quality factor Q and finally influence the focus resolution and the position accuracy of the focus spot [41], or linked to the experimental difficulties to tune media parameters and to obtain fine observations.

The objective of this work is to show that it is possible to model and reproduce these observations with only the standard acoustic wave equation in 2-D but associated with a specific fine scale description of a heterogeneous medium producing Helmholtz resonance. To do so, we rely on the Spectral Element Method (SEM) to solve the

acoustic equation in the time domain [42, 43, 44, 45]. The spectral element method is a powerful tool which has the flexibility and accuracy to handle strongly discontinuous with complex unstructured meshes, meanwhile offering a spectral convergence with the polynomial degree, leading to a very low dispersion, and still very efficient thanks to its diagonal mass matrix, its explicit time scheme and parallel implementation. Numerical modeling makes it possible to flexibility control all relevant parameters of the experiment and measure all physical quantities such as pressure or particle displacement anywhere in the domain, opening the door to a better understanding of this phenomenon.

The article is organized as follows: in section 2 the basic theory of time-reversal acoustics and its SEM implementation are described. In Section 3, we observe the focusing phenomenon submitted to the diffraction limit in two simple homogeneous media. Then, we introduce heterogeneities with split ring shape of subwavelength size. We show that, even if only simple physics is used at the subwavelength scale, once these fine scale structures have been introduced, Helmholtz resonance and frequency band-gaps can be easily observed. From the numerical method perspective, such a modeling is only possible thanks to the very low dispersion and meshing flexibility offered by SEM. Then, in such media, focusing spots with a resolution below the diffraction limit are observed. Finally, in Section 4, we offer some physical interpretations of our observations.

2. Acoustic time reversal equations and numerical implementation

In the present section, we briefly recall the acoustic wave and the time reversal equations. Then an overview of the numerical scheme of the Spectral Element Method (SEM) and a description of the time reversal implementation are given. The description and the experiments are done in a 2-D framework but would remain valid in 3-D.

2.1. The acoustic equations

For an acoustic domain $\mathbf{\Omega}$, for all positions $\mathbf{x} = (x, z)$ and any time t, the fluid velocity potential $q(\mathbf{x}, t)$ is solution of :

$$\begin{aligned} &\frac{1}{\kappa}\ddot{q} - \boldsymbol{\nabla}\cdot\dot{\mathbf{u}} = f \ , \\ &\dot{\mathbf{u}} = \frac{1}{\rho}\boldsymbol{\nabla} q \ , \end{aligned} \tag{1}$$

where $\kappa(\mathbf{x})$ is the acoustic bulk modulus, $\rho(\mathbf{x})$ is the (mass) density, $\mathbf{u}(\mathbf{x}, t)$ is the displacement vector, $\dot{\mathbf{u}}(\mathbf{x}, t)$ is the velocity vector and $f(\mathbf{x}, t)$ is a scalar external source term. Since $\mathbf{\Omega}$ is unbounded (to avoid any reflections at the boundary), a radiation boundary condition is imposed to the infinity (Sommerfield condition). Note that the acoustic pressure p is directly proportional to $\dot{q}$.

2.2. Time reversal and the diffraction limit

According to the representation theorem [46, 1], for a given acoustic subdomain $\mathbf{V}$ in $\mathbf{\Omega}$ of boundary S (see Fig. 1a), for any $\mathbf{x} \in \mathbf{V}$, assuming zero initial condition, we have:

$$\begin{aligned} q(\mathbf{x}, t) = &\int_{-\infty}^{\infty} d\tau \int_{\mathbf{V}} f(\mathbf{x}', \tau) G(\mathbf{x}, t-\tau; \mathbf{x}') \, d\mathbf{\Omega}' \\ &+ \int_{-\infty}^{\infty} d\tau \oint_{S} \frac{1}{\rho} \left[\boldsymbol{\nabla}' q(\mathbf{x}', \tau) G(\mathbf{x}, t-\tau; \mathbf{x}') - q(\mathbf{x}', \tau) \boldsymbol{\nabla}' G(\mathbf{x}, t-\tau; \mathbf{x}') \right] \cdot \mathbf{n} \, dS' \end{aligned} \tag{2}$$

where $G(\mathbf{x}, t; \mathbf{x}')$ is the Green function, solution of Eq. (1) for $f = \delta(\mathbf{x} - \mathbf{x}')\delta(t)$, δ the Dirac distribution, $\boldsymbol{\nabla}'$ the gradient operator with respect to $\mathbf{x}'$ coordinates, $\mathbf{n}$ the outward normal to S, $d\mathbf{\Omega}'$ and dS' indicate that the integrals are computed for the $\mathbf{x}'$ variable.

A time reversal experiment (numerical or not) is performed in two steps, the forward and the backward steps:

- In the forward step, a source f (usually localized in time and space) is triggered at time t_0. For the sake of simplicity, we assume in this section that $t_0 = 0$. The velocity potential q_d can be then obtained for any location $\mathbf{x}$ and time t, using

the first part of the representation theorem (Eq. (2)):

$$q_d(\mathbf{x},t) = \int_{-\infty}^{\infty} d\tau \int_{\mathbf{V}} f(\mathbf{x}',\tau) G(\mathbf{x},t-\tau;\mathbf{x}')\, d\mathbf{\Omega}' \,. \tag{3}$$

During this first stage, q_d and $\boldsymbol{\nabla} q_d$ are recorded on the contour S until a time T is reached such that all the energy is gone from $\mathbf{V}$, that is, for any location $\mathbf{x}$ in $\mathbf{V}$, $q_d(\mathbf{x},T) = 0$ and $\boldsymbol{\nabla} q_d(\mathbf{x},T) = \mathbf{0}$.

- In the backward step, q_d and $\boldsymbol{\nabla} q_d$ are time reversed and sent back in $\mathbf{\Omega}$ from S using the second part of the representation theorem to obtain the reversed velocity potential:

$$q_r(\mathbf{x},t) = \int_{-\infty}^{\infty} d\tau \oint_S \frac{1}{\rho} \left[\boldsymbol{\nabla}' q_d(\mathbf{x}',T-\tau) G(\mathbf{x},t-\tau;\mathbf{x}') - q_d(\mathbf{x}',T-\tau)\boldsymbol{\nabla}' G(\mathbf{x},t-\tau;\mathbf{x}')\right]\cdot\mathbf{n}\, dS' \tag{4}$$

It can be shown that [19],

$$q_r(\mathbf{x},t) = q_d(\mathbf{x},T-t) - q_d(\mathbf{x},t-T)\,. \tag{5}$$

Similarly, in terms of pressure (because $p \propto \dot{q}$):

$$p_r(\mathbf{x},t) = -p_d(\mathbf{x},T-t) - p_d(\mathbf{x},t-T) \tag{6}$$

The back-propagated wavefield q_r is therefore the sum of the direct wavefield reversed in time and shifted by T, $q_d(\mathbf{x},T-t)$, and minus the direct wavefield shifted by T, $q_d(\mathbf{x},t-T)$. This means that the back-propagated wavefield q_r first shows a collapse of the wavefield toward the source location until the collapse time T is reached and then a diverging field equal to the direct wavefield q_d but negative and delayed by T. Because of the near-field, the direct field q_d spot size at the origin time and position is much smaller than the wavelength and even singular in the case of a point source f. For q_r, the sum of converging and diverging field at collapsing time leads to the diffraction limit: the size of the focusing spot is no smaller than half the wavelength. Obtaining a focusing spot smaller than half the wavelength is a so-called subwavelength focusing, which is the object of the numerical experiments of this work.

2.3. Spectral element numerical implementation

SEM [42, 43, 44, 45] is a finite element method that solves the weak form of Eq. (1) in the time domain: for all admissible test function w, the following equation needs to be satisfied:

$$m\left(w,\ddot{q}\right)+a(w,q)=\left(w,f\right), \tag{7}$$

where

$$\begin{aligned} m\left(w,\ddot{q}\right) &= \int_{\mathbf{\Omega}} \frac{1}{\kappa} w\ddot{q}\, d\mathbf{\Omega}\,, \\ a(w,q) &= \int_{\mathbf{\Omega}} \frac{1}{\rho} \boldsymbol{\nabla} w \cdot \boldsymbol{\nabla} q\, d\mathbf{\Omega}\,, \\ \left(w,f\right) &= \int_{\mathbf{\Omega}} f w\, d\mathbf{\Omega}\,. \end{aligned}$$

Compared with classical low degree finite elements, SEM is based on a tensorised high degree polynomial approximation per element, combined with precise numerical quadrature linked to the so-called Gauss-Lobatto-Legendre (GLL) points. As a consequence, SEM displays some interesting characteristics, important for the numerical experiments presented in this article :

- it has a spectral convergence with the element polynomial degree leading to a very low dispersion, allowing very long signal modeling with a high accuracy;
- the mass matrix is exactly diagonal, making it possible to use efficiently explicit time scheme;
- it can handle any kind of material discontinuities (including solid-fluid).

However, the SEM has one critical drawback: the mesh need to be based on quadrilateral (in 2-D) or hexahedron (in 3-D) elements. This is not a problem in 2-D, but in 3-D the hexahedron meshes can be very difficult to generate for complex structures.

The only specificity of our experiments is the need to introduce the S contour integral of Eq. (4) in SEM to obtain the reversed wavefield q_r. In order to compute this contour integral, we rely on the simplest possible quadrature: S is represented by discret set of equally spaced points $\mathbf{x}_s$, $s \in 1,..,N$ associated width a contour length (or

surface in 3-D) dS. N is chosen to obtain 10 points per wavelength of the direct wavefield. Once S is discretized, the reversed field q_r given by Eq. (4) can be associated to the solution of the Eq. (1) for a source

$$f_r(\mathbf{x},t) = \sum_{s=1,N} \frac{dS}{\rho(\mathbf{x}_s)} \left[\boldsymbol{\nabla} q_d(\mathbf{x}_s, T-t)\delta(\mathbf{x}-\mathbf{x}_s) + q_d(\mathbf{x}_s, T-t)\boldsymbol{\nabla}\delta(\mathbf{x}-\mathbf{x}_s)\right]\cdot\mathbf{n}\,. \tag{8}$$

Such a source presents no difficulty for SEM and the source term (w, f) in Eq. (7) for $f = f_r$ is introduced the same way it is done for any classical point source (the only difference with classical SEM usage is that there are 2 sources at N locations at the same time).

In practice, to perform a time reversal experiment, SEM is used a first time to compute the direct wavefield and to record q_d and $\boldsymbol{\nabla} q_d$ at the $\mathbf{x}_s$ point set. Using SEM a second time, these records are then time reversed and sent back in $\boldsymbol{\Omega}$ as sources according to Eq. (9) to obtain q_r.

Note that another elegant and efficient solution to implement TRM, based on the direct discrete differentiation of the forward wavefield, has been presented by [47].

3. Numerical Experiments

In this section, we first validate the numerical time reversal method elaborated in the previous section in simple media. Then, after presenting a direct modeling of Helmholtz resonators, we perform numerical time reversal experiments in resonating media, displaying the subwavelength focusing phenomenon.

3.1. Focusing at the diffraction limit in homogeneous media

The method is tested in the numerical set up presented in Fig. 1b. It is a domain of $30 \times 30\, m^2$, filled with air ($V_p = \sqrt{\kappa/\rho} = 343.6\, ms^{-1}$, $\rho = 1.2\ kg\ m^{-3}$). To prevent reflections caused by the scattering of waves from the domain boundaries, perfectly matched layers (PML) absorbing boundaries are implemented all around the domain [48]. The source is placed in the center of the domain. Around the source, a $5 \times 5\, m^2$ square box area in which a different medium from the surrounding air can be used. The TRM is arranged to form a circular cavity with a radius of $12.5m$. Note that the

circular geometry of the TRM is irrelevant to the focusing results shown below. The same results would be obtained for an arbitrary closed shape TRM in the far field of the source.

The source term has the following form:

$$f(\mathbf{x},t) = \delta(\mathbf{x}-\mathbf{x}_0)g(t)\,, \tag{9}$$

where $\mathbf{x}_0$ is the source location and the time function $g(t)$ is Ricker wavelet (i.e. second derivative of a Gaussian function, see Fig. 2a) with a central frequency $f_0 = 110\ Hz$, corresponding roughly to a maximum frequency $f_{max} = 300\ Hz$ (see Fig. 2b). Note that computing accurately the wavefield in the vicinity of such a point source imposes a denser mesh than usual near $\mathbf{x}_0$. Nevertheless, computing accurately the near-field is only necessary to visualize it but is not necessary to compute accurately the far-field. More details about this point can be found in Appendix A.

Two kinds of media are used in the embedded $5 \times 5\,m^2$ square box:

1. the air. In this case the $\mathbf{\Omega}$ is fully homogeneous, with a dominant wavelength $\lambda \simeq 3m$;
2. an anisotropy medium with bulk modulus $\kappa = 141673Pa$ (the same to that of the air), with two velocities, $v_1 = 343.6m\ s^{-1}$ for the horizontal direction and $v_2 = 56.6m\ s^{-1}$ for the vertical direction associated to two dominant wavelengths, $\lambda_1 \simeq 3m$ and $\lambda_2 \simeq 0.5m$ respectively. Note that a standard fluid with a scalar density ρ cannot be anisotropic, nevertheless, introducing a density matrix allows for anisotropic fluid (See Appendix B for more details).

For the two models, we compute the acoustic pressure p for both forward and time-reversed steps described in section 2.2. Snapshots of both p_d and p_r at different time steps are shown in Fig. 3. Pressure field cross-sections through the source location along the $x - x'$ and $z - z'$ directions at the forward origin time (t_0) are shown in Fig. 4a and at the time-reversal focus time ($T - t_0$) are shown in Fig. 4c. It can be seen that, in both cases, $p_d(\mathbf{x},t)$ and $p_r(\mathbf{x},T-t)$ have an opposite sign but the same spatial shape, which is predicted by Eq. (6), except for the focusing time (around $t = T - t_0$).

For the homogeneous case (case 1), from the snapshots and the cross-sections of the direct wavefield at $t = t_0$ shown in Figs. 3a and 4a, we can clearly see the very

narrow isotropic source spot (almost singular) related to the source near-field. For the time reversed wavefield, the isotropic focusing spot is also clearly visible at $t = T - t_0$ (see the wavefield snapshots and cross-sections in Fig. 3b and 4c), but, as expected, its width corresponds approximately to the diffraction limit $\lambda/2$.

For the anisotropic media (case 2), the waves travel faster in the x direction than in the z direction, leading to an elliptic wavefront (see Fig. 3c, top panel). Moreover, the wavefield is more complex because of the reflection and diffraction at the boundaries between the anisotropy and the isotropy media (see Fig. 3c, middle and bottom panels). Nevertheless, a clean elliptic focus spot is observed for the time reversal experiment (see Fig. 3d, bottom panel). Similarly to the homogeneous case, the focusing spot reaches the diffraction limit. Besides, due to anisotropy, the diffraction limits is more complex than for the isotropic case: it has different width in each direction ($\sim \lambda_1/2$ along x and $\sim \lambda_2/2$ along z), as shown in the cross-sections in Figs. 4b and 4d.

The anisotropic case shows one of the ambiguity on the focusing spot size that often leads to confusion: if measured along the z axis, the focusing spot is of size $\lambda_2/2$, which is much smaller than the focusing spots obtained in the air medium. One could draw the wrong conclusion that the diffraction limit is beaten, at least in one direction. This is obviously not the case: when computed with the velocities of the medium in the vicinity of the source location, the focusing spot size is exactly the one predicted by the diffraction limit.

It should be mentioned that it is sometimes written that, from a purely numerical point of view, computational time reversal modeling can exactly reproduce the direct wavefield, leading to an "exact reversibility" [49] . This could be potentially misleading as it seems to contradict the results we are showing here. Nevertheless, this "exact reversibility" is obtained with admissible initial conditions as a source and not with a more physical external source term f such as the one used in this work (see Eq. 9). We believe that such admissible initial condition "sources" can only produce a propagating wavefield and cannot model physical sources generating a near-field. Indeed, based on initial conditions, the source far-field maximum frequency cannot be controlled for an arbitrary small size source, and controlling independently both the maximum frequency and the spatial extent of the source is necessary to model physical sources. As the $\lambda/2$

diffraction limit is directly related to the source near-field, there is no contradiction.

Finally, these two simple experiments show the validity and precision of our modeling approach.

3.2. Subwavelength focusing in media with Helmholtz resonator inclusions

Subwavelength focusing is mostly observed in some very specific media: resonating metamaterial media [31, 41, 50]. In this section, we first check that the Helmholtz resonator behavior can be fully reproduced with our modeling scheme. Then, time reversal experiments are performed in media that includes Helmholtz resonators (resonating media).

3.2.1. Helmholtz resonator modeling

A Helmholtz resonator produces an acoustic resonance by a process analogous to the oscillation of a mass-spring oscillator. It must contain a neck connected to a cavity filled with a larger volume of air. The larger volume of air acts as the spring, while the neck act as the mass. According to the specific shape of Helmholtz resonator used in this work (see below and Fig. 5a), and the formula given, for example, by [51], the natural frequency is approximately:

$$f_H \simeq \frac{V_p}{2\pi}\sqrt{\frac{A}{VL}}, \tag{10}$$

where A is the cross-sectional area of the neck, V is the volume of the cavity, L is the length of the neck, V_p is the velocity of the air. For 2-D Eq. (10) becomes:

$$f_H \simeq \frac{V_p}{2\pi}\sqrt{\frac{d}{\pi(r^2 l)}}, \tag{11}$$

where l is the length of the neck, r is the diameter of the ring, d is the width of the neck.

To numerically model a Helmholtz resonator, we mesh a split ring made of aluminum, with a density of 2700 $kg\ m^{-3}$, and velocity 5000 ms^{-1} (see Fig. 5a). The mesh design of resonator complex and fine structure is done thanks to the mesh software CUBIT. The ring has $r = 8.5cm$, $d = 0.3cm$, and $l = 1.1cm$, which, according to Eq. (11) the resonance frequency is about $383Hz$.This is consistent with the numerical experiment: using a broadband source with a central frequency of $300Hz$ inside

the ring, the pressure signal recorded outside the ring (Figs. 6a and 6c) shows a clear low frequency resonance of about $390Hz$. This frequency is much lower than the first eigenfrequency of an air filled closed cavity of the same size (about $4040Hz$) and consistent with the one predicted by Eq. (11). Based on this, we conclude that the Helmholtz resonator can be successfully modeled by SEM thanks to an appropriate mesh and medium properties.

3.2.2. Time reversal experiments in resonating media

In this section, we consider two time reversal experiments: in the first one, a single ring is used and in the second, a multiple ring net is used. Each of these two experiments is performed twice: one with a source central frequency close to the Helmholtz resonant frequency and one with a much lower source central frequency.

We first consider a single ring located in the middle of a $8 \times 8\, m^2$ model area. We perform three experiments with each time a different source location (see source 1, 2 and 3 in Fig. 5a). Source 1 is inside the ring, source 2 is to the right side of the ring, and source 3 above the exit of the ring. The distances between the three positions are all in sub-wavelength range ($\sim \lambda/13$). A broadband source is used with a central frequency of $300Hz$, which is close to the natural frequency of the ring. All three sources lead to a strong resonance and almost a monochromatic signal outside the ring (Fig. 7a). However, when the recorded signals are time-reversed and send back to their original positions, interestingly and unlike the single soda can experiments shown in the Supplementary material of [30], we can here identify the three different focus spots according to its position. From the cross-section we can clearly see the differences (Fig. 8a): for source 1 and 3 both a narrow focusing spot with a width of the diameter of the ring is observed ($\sim \lambda/13$) ; for source 2 the focus spot is not narrow but disturbed by the ring. Even with noisy data, it would be simple to make the difference between source 1 or 3 from source 2, which is sub-wavelength source localization.

We then perform the same experiment with a periodic ensemble of 7×7 rings arranged on a square matrix as shown in Fig. 5b. Since all the rings have the same natural frequency and are spatially very close to each other (the spacing between rings is much smaller than λ), coupling between resonators can be observed leading to a

complex signal at the TRM as shown in Figs. 6b and 6d. Interestingly, the observed and predicted [52, 53] forbidden frequency band, or band gap, $(400Hz - 600Hz)$ can be observed in the signal spectra (Fig. 6d). The coupling between the 7×7 rings leads to a much longer resonance signals than the single ring case. Therefore it takes a very long time (T) to let all the acoustic energy out of the TRM contour S, which significantly increase the computing time. Fortunately, the resonance attenuates to a relatively small amplitude after $1s$ (see Figs. 6b) and we choose to truncate signals to $T = 1s$. This nevertheless leads to an imperfect time reversal experiment and explains the spurious waves outside of the TRM contour in Fig. 7d. Compared to the single ring case, the observed focusing spot is slightly different (see Figs. 7d and 8b). Nevertheless, as it can be seen from the cross-sections (Fig. 8b), these differences do not change the main conclusion: it is obvious that the acoustic pressure field focus back to the ring where the source was triggered, even if a small amount of pressure can be measured in the neighbor rings. Finally, two sources in two adjacent rings are used (see Fig. 5b). As observed from the back-propagated field at focusing time cross-sections (Fig. 8b), source 1 and 2 can be very clearly differentiated. This once again shows that a subwavelength focusing has been achieved. This result is consistent with that of the sound experiment shown by [30].

Finally, we show that, in order to obtain a subwavelength focusing in our time reversal experiments, it is important that the source frequency band contains the Helmholtz resonant frequency of the split ring. If we use a lower source central frequency $f_0 = 120Hz$, which is two times smaller than the natural frequency of the ring, and perform similar time reversal experiments to the one done above with one ring and multiple rings (12×12), nearly no resonance can be observed in the far field. With such a low frequency source, no subwavelength focusing can be observed for the one ring case (Figs. 9a and 9c). For the multiple rings case, the observed focus spot size is about $\lambda/4$ (Fig. 9d) which is below the theoretical diffraction limit in the air. Even if the focusing spot is not as small as the one observed for $f_0 = 300Hz$, this could be considered as a subwavelength focusing. Nevertheless, as it will be shown in the next section, this not the case.

4. Discussion and Conclusions

4.1. Non-periodic homogenization and effective medium

For a better understanding of the results obtained in Section 3.2, we use the non-periodic homogenization [54, 55, 56, 57] to compute the effective medium "seen" by the wavefield.

The non-periodic homogenization is an operator $\boldsymbol{\mathcal{H}}^{\varepsilon_0}$ that, for a given medium $(\kappa(\mathbf{x}), \rho(\mathbf{x}))$ and a given wavefield propagating in that medium with a minimum wavelength λ_{min} , makes it possible to compute the effective medium

$$(\kappa^*(\mathbf{x}), \mathbf{L}^*(\mathbf{x})) = \boldsymbol{\mathcal{H}}^{\varepsilon_0}(\kappa, \rho) \ , \tag{12}$$

where $\mathbf{L}^*$ is a density matrix that can carry anisotropy (see Appendix A). The effective medium depends on the parameter ε_0:

$$\varepsilon_0 = \frac{\lambda_0}{\lambda_{\text{min}}} \ , \tag{13}$$

where λ_0 is a user defined scale: it is the limit between what the user desire to consider as small scales and as large scales. In practice, $\lambda_0 = 0.5\lambda_{\text{min}}$ ($\varepsilon_0 = 0.5$) is often a good choice for many media, but it can be a smaller value depending on the demanded accuracy and the specific medium considered (as for most asymptotic methods, only the convergence of the solution as a function of ε_0 is warrantied). The objective of the homogenization process is to remove the small scales and to keep the large scales in a consistent way with the wave equation solution. Depending on ε_0, the effective wavefield computed in the effective medium $(\kappa^*, \mathbf{L}^*)$ is the same as the reference wavefield (computed in the original medium) up to the desired accuracy with a convergence as ε_0^2 [56]. The non-periodic homogenization process is similar to the classical two scale periodic homogenization applied to wave propagation problems [58], but is not bounded to periodic medium, and specifically designed for deterministic medium with no natural scale separation. It has mainly two differences compared to the classical two scale periodic homogenization: firstly, the resulting effective medium is not spatially constant (it varies with $\mathbf{x}$, but is smoother than the original medium); secondly, for a fixed ε_0, it depends on the maximum frequency of the source (through λ_{min}).

In practice, the non-periodic homogenization is often used as a pre-processing tool to simplify a complex medium before solving the wave equation (see [59] for example). But here, it has another application: the non-periodic homogenization process makes it possible to upscale the medium to the wavefield scale and reveals how the medium is perceived by the wavefield for a particular λ_{min} and therefore for a particular source frequency. This is very useful because this upscaling phenomenon is a non-linear process that can lead to counter intuitive effects. Indeed, for the experiments in Section 3.2, one could think that, as the ring(s) area is a compound medium of the background air and a faster medium (aluminum), the effective velocity in this area should be slightly faster than the air. The homogenization process shows a completely different result. Applied to our rings for the $100Hz$ source (see Fig. 10), it can be seen that the effective velocity in the rings area is two times slower than the surrounding air. This effective low velocity in the ring area explains the observed focusing spot size: while it is twice smaller than the theoretical diffraction limit in the air, it corresponds exactly to the diffraction limit for the computed effective velocity of the ring area. Therefore, in that case, the observations do not correspond to subwavelength focusing. This result is consistent with asymptotic mathematical analysis preformed in periodic settings [60] or with random heterogeneities [61]. It is also consistent with a result obtained with random slow velocity inclusions with the fast multipole method [62]. This later work is nevertheless less spectacular than ours with Helmholtz inclusions: indeed, obtaining a slow velocity area and therefore a smaller focusing spot with slow velocity inclusions is intuitively expected whereas with Helmholtz inclusions, which imply a mixing of the background medium (the air) with faster inclusion (the aluminum), we could intuitively expect a faster effective medium and therefore a larger focusing spot where the opposite is observed.

Unfortunately, the same non-periodic homogenization process cannot be applied to the $300Hz$ source. When reaching the resonance frequency, the medium dispersion relation becomes singular [53] and the wavefield no longer exhibits any minimum wavelength. This breaks the main hypothesis of homogenization and makes any interpretation of the obtained effective medium beyond that frequency difficult (the effective $\mathbf{L}^*$ becomes locally negative). This confirms that Helmholtz resonance is the

critical point to obtain a subwavelength focusing. Nevertheless, it raises the question of subwavelength focusing's definition: what is $\lambda/2$ when the effective wavelength is locally undefined? It indicates that it is probably possible to reconcile subwavelength observations with the diffraction limit, but this remains to be precisely established. The importance of a network of Helmholtz resonators has been established mathematically by [63]. Our numerical results nevertheless go a bit further as it appears to be possible to observe sub-wavelength focusing with a single Helmholtz resonator.

4.2. Conclusions

In this work, we have proposed to apply the Spectral element method to model the time-reversal focusing of 2-D acoustic waves. We have first shown that with a simple split ring shape heterogeneity, it is possible to model the Helmholtz resonance phenomena, as well as frequency band gaps by combining several split rings. Performing numerical time reversal experiments in media containing one or more Helmholtz resonators, we have shown it is possible to observe the so-called subwavelength focusing, provided that the source central frequency is close to the resonant frequency. We have observed a $\lambda/13$ focusing spot size in the single resonant split ring and multiple resonant split rings experiments, where $\lambda/13$ corresponds to the dimension of one Helmholtz resonator. Thanks to the non-periodic homogenization tool, we have shown that, if the sources central frequency is much lower than the Helmholtz resonant frequency, the observed $\sim \lambda/4$ focusing spot doesn't correspond to subwavelength focusing but to the diffraction limit for the local minimum wavelength computed in the effective medium of the compound medium of the rings and the air.

From the numerical point of view, this work shows that numerical schemes such as SEM are stable and precise enough to reproduce Helmholtz resonance, band gaps and finally subwavelength focusing, which, to our best knowledge, has not been done before. From the physical world point of view, our work shows that, in order to observe subwavelength focusing, only very simple physics (the standard acoustic wave equation) and small scale scattering heterogeneities with a specific shape is required. Moreover, if it is often argued both experimentally and theoretically [30, 63] that a combination of several sub-wavelength resonators is necessary to observed a sub-wavelength

focusing phenomenon, our numerical modeling experiments suggest that it is possible to observe such a phenomenon with a single resonator.

As to the existence of sub-wavelength focusing, a definitive answer is probably out of reach at this stage and is subject to interpretation. Because Helmholtz resonators do not show a macroscopic effective minimum wavelength for frequencies close to the resonance frequency, in such cases the definition of near-field evanescent waves smaller than half wavelength loses its meaning. Therefore, on one hand, sub-wavelength focusing probably does not exist. Nevertheless, on the other hand, in practice, the focusing spot reaches the size of the Helmholtz resonator, which is much smaller than the wavelength of the surrounding media and is impossible to achieve with classical media. In that perspective, Helmholtz resonators display a phenomenon as useful and intriguing as sub-wavelength focusing.

This work open the door to a better and simpler understanding of sub-wavelength focusing phenomenon. Indeed, if experimental work can be difficult to set up, numerical modeling are very simple and makes it possible to access any physical quantities anywhere, anytime.

Acknowledgement

The computations were performed on the CCIPL computer "Erdre". This work was funded by the China Scholarship Council and the Pays de la loire, France. We thank A. Fichtner, D. Givoli, and another anonymous reviewer for providing constructive comments and suggestions that improved the manuscript.

Appendix A. About the point source and the spectral element method

The fact that the Dirac function $\delta(\mathbf{x}-\mathbf{x}_0)$ in the source term (9) cannot be accurately expended on the polynomial basis embedded in the spectral element method often leads to the conclusion that the source is somehow spatially low-pass filtered by the polynomial basis. This is not wrong, but we prefer to present this aspect in a different way. In order to be accurate, for SEM as for any finite element method, it is necessary that:

1. integrals in each term of Eq. (7) must be precisely computed;
2. the exact solution to the considered equations is correctly approximated by its projection on the spectral element basis.

About the first point, for a point source, the source term can always be exactly integrated, whatever the chosen spectral element basis is:

$$(w,f)=\int_{\mathbf{\Omega}} w(\mathbf{x})\delta(\mathbf{x}-\mathbf{x}_0)g(t)\,d\mathbf{\Omega}=w(\mathbf{x}_0)g(t)\,, \tag{A.1}$$

and therefore no difficulty can be expected from this point. For the second point, the spectral element basis setup (basically estimating the size and degree of the elements) is usually based on an estimate of the minimum wavelength of the far-field calculated from the maximum frequency of the source and on the minimum wavelength of the medium. Nevertheless, the near-field of a point source is singular and cannot be correctly expended on any classical polynomial basis, and we expect an error near the source at least. Interestingly, because the near-field carries no energy and decays very rapidly with the distance to the source [1], it has no consequence on the far-field and only the wavefield in the element containing the source is affected. If accurately computing the near-field is necessary, as it is the case here, one can simply increase the density of element near the source, keeping in mind that the element containing the source will never accurately represent the near-field (but only this one). For example, to obtain Fig. 4a, the element size close to the source are about $\lambda/40$ and therefore, the picture is accurate everywhere but exactly at the source, which has (almost) no visual effect.

Appendix B. Anisotopy in fluid

To allow anisotropy in acoustic media, instead of the classical acoustic constitutive relation

$$\dot{\mathbf{u}} = \frac{1}{\rho}\boldsymbol{\nabla} q\,, \tag{B.1}$$

we can use the following more general relation

$$\dot{\mathbf{u}} = \mathbf{L}\cdot\boldsymbol{\nabla} q\,, \tag{B.2}$$

where $\mathbf{L}$ is the density matrix. Such a density matrix naturally appears when upscaling media with fine structures compared to the wavelength [45]. If for classical isotropic acoustic media $L_{ij}(\mathbf{x}) = \delta_{ij}/\rho(\mathbf{x}), (i,j=1,2)$, where δ_{ij} the Kornecker symbol, for more general media, $\mathbf{L}$ may be less simple and allows anisotropy.

References

[1] K. Aki, P. Richards, Quantitative Seismology: Theory and Methods., Freeman, San Francisco., 1980.

[2] A. Derode, P. Roux, M. Fink, Robust acoustic time reversal with high-order multiple scattering, Phys. Rev. Lett. 75 (23) (1995) 4206.

[3] M. Fink, Time-reversed acoustics, Sci. Am. 281 (5) (1999) 91–97.

[4] M. Fink, D. Cassereau, A. Derode, C. Prada, P. Roux, M. Tanter, J.-l. Thomas, F. Wu, Time-reversed acoustics, Rep. Prog. Phys. 63 (12) (2000) 1933.

[5] J.-P. Fouque, J. Garnier, A. Nachbin, K. Sølna, Time-reversal refocusing for point source in randomly layered media, Wave Motion 42 (3) (2005) 238–260.

[6] S. D. Santos, Z. Prevorovsky, Imaging of human tooth using ultrasound based chirp-coded nonlinear time reversal acoustics, Ultrasonics 51 (6) (2011) 667 – 674.

[7] A. Derode, A. Tourin, M. Fink, Random multiple scattering of ultrasound. ii. is time reversal a self-averaging process?, Phys. Rev. E: Stat., Nonlinear, Soft Matter Phys. 64 (3) (2001) 036606.

[8] P. Kosmas, C. M. Rappaport, Time reversal with the fdtd method for microwave breast cancer detection, Microwave Theory and Techniques, IEEE Transactions on 53 (7) (2005) 2317–2323.

[9] A. Derode, A. Tourin, J. de Rosny, M. Tanter, S. Yon, M. Fink, Taking advantage of multiple scattering to communicate with time-reversal antennas, Phys. Rev. Lett. 90 (1) (2003) 014301.

[10] G. Lerosey, J. De Rosny, A. Tourin, A. Derode, G. Montaldo, M. Fink, Time reversal of electromagnetic waves, Phys. Rev. Lett. 92 (19) (2004) 193904.

[11] S. Catheline, N. Benech, J. Brum, C. Negreira, Time reversal of elastic waves in soft solids, Phys. Rev. Lett. 100 (6) (2008) 064301.

[12] C. S. Larmat, R. A. Guyer, P. A. Johnson, Time-reversal methods in geophysics, Phys. Today 63 (8) (2010) 31–35.

[13] C. Larmat, J.-P. Montagner, Y. Capdeville, W. Banerdt, P. Lognonné, J.-P. Vilotte, Numerical assessment of the effects of topography and crustal thickness on martian seismograms using a coupled modal solution–spectral element method, Icarus 196 (1) (2008) 78–89.

[14] C. Larmat, J.-P. Montagner, M. Fink, Y. Capdeville, A. Tourin, E. Clévédé, Time-reversal imaging of seismic sources and application to the great sumatra earthquake, Geophys. Res. Lett. 331 (19) (2006) 1–4.

[15] J.-P. Montagner, C. Larmat, Y. Capdeville, M. Fink, H. Phung, B. Romanowicz, E. Clévédé, H. Kawakatsu, Time-reversal method and cross-correlation techniques by normal mode theory: a three-point problem, Geophys. J. Int. 191 (2) (2012) 637–652.

[16] W. C. Elmore, M. A. Heald, Physics of waves, Courier Corporation, 1969.

[17] M. Born, E. Wolf, Principles of Optics, 7th Edition, Cambridge University Press, 1999.

[18] D. Cassereau, M. Fink, Time-reversal of ultrasonic fields. iii. theory of the closed time-reversal cavity, Ultrasonics, Ferroelectrics, and Frequency Control, IEEE Transactions on 39 (5) (1992) 579–592.

[19] M. Fink, Time-reversal waves and super resolution, in: Journal of Physics: Conference Series, Vol. 124, IOP Publishing, 2008, p. 012004.

[20] J. Li, C. T. Chan, Double-negative acoustic metamaterial, Phys. Rev. E: Stat., Nonlinear, Soft Matter Phys. 70 (2004) 055602.

[21] J. Pendry, Negative refraction makes a perfect lens, Phys. Rev. Lett. 85 (2000) 3966–3969.

[22] R. A. Shelby, D. Smith, S. Schultz, Experimental verification of a negative index of refraction, Science 292 (2001) 77.

[23] D. R. Smith, J. B. Pendry, M. C. Wiltshire, Metamaterials and negative refractive index, Science 305 (5685) (2004) 788–792.

[24] Z. Liu, H. Lee, Y. Xiong, C. Sun, X. Zhang, Far-field optical hyperlens magnifying sub-diffraction-limited objects, Science 315 (5819) (2007) 1686–1686.

[25] X. Zhang, Z. Liu, Superlenses to overcome the diffraction limit, Nat. Mater. 7 (6) (2008) 435–441.

[26] P. Blomgren, G. Papanicolaou, H. Zhao, Super-resolution in time-reversal acoustics, J. Acoust. Soc. Am. 111 (1) (2002) 230–248.

[27] J.-P. Fouque, J. Garnier, K. Sølna, Time reversal super resolution in randomly layered media, Wave Motion 43 (8) (2006) 646–666.

[28] J. de Rosny, M. Fink, Overcoming the diffraction limit in wave physics using a time-reversal mirror and a novel acoustic sink, Phys. Rev. Lett. 89 (2002) 124301.

[29] G. Lerosey, J. de Rosny, A. Tourin, M. Fink, Focusing beyond the diffraction limit with far-field time reversal, Science 315 (5815) (2007) 1120–1122.

[30] F. Lemoult, M. Fink, G. Lerosey, Acoustic resonators for far-field control of sound on a subwavelength scale, Phys. Rev. Lett. 107 (2011) 064301.

[31] F. Lemoult, G. Lerosey, J. de Rosny, M. Fink, Resonant metalenses for breaking the diffraction barrier, Phys. Rev. Lett. 104 (2010) 203901.

[32] N. Fang, D. Xi, J. Xu, M. Ambati, W. Srituravanich, C. Sun, X. Zhang, Ultrasonic metamaterials with negative modulus, Nat. Mater. 5 (6) (2006) 452–456.

[33] S. Zhang, L. Yin, N. Fang, Focusing ultrasound with an acoustic metamaterial network, Phys. Rev. Lett. 102 (19) (2009) 194301.

[34] M. Fink, F. Lemoult, J. de Rosny, A. Tourin, G. Lerosey, Subwavelength focussing in metamaterials using far field time reversal, Springer, 2013.

[35] A. Song, M. Badiey, A. E. Newhall, J. F. Lynch, H. A. DeFerrari, B. G. Katsnelson, Passive time reversal acoustic communications through shallow-water internal waves, Oceanic Engineering, IEEE Journal of 35 (4) (2010) 756–765.

[36] G. Zhang, J. M. Hovem, H. Dong, L. Liu, Coherent underwater communication using passive time reversal over multipath channels, Appl. Acoust. 72 (7) (2011) 412–419.

[37] A. Sentenac, P. C. Chaumet, Subdiffraction light focusing on a grating substrate, Phys. Rev. Lett. 101 (1) (2008) 013901.

[38] G. Shvets, S. Trendafilov, J. Pendry, A. Sarychev, Guiding, focusing, and sensing on the subwavelength scale using metallic wire arrays, Phys. Rev. Lett. 99 (5) (2007) 053903.

[39] G. Bartal, G. Lerosey, X. Zhang, Subwavelength dynamic focusing in plasmonic nanostructures using time reversal, Phys. Rev. X 79 (20) (2009) 201103.

[40] A. Maznev, G. Gu, S.-y. Sun, J. Xu, Y. Shen, N. Fang, S.-y. Zhang, Extraordinary focusing of sound above a soda can array without time reversal, New J. Phys. 17 (4) (2015) 042001.

[41] F. Lemoult, M. Fink, G. Lerosey, Far-field sub-wavelength imaging and focusing using a wire medium based resonant metalens, Wave. Random. Complex. 21 (4) (2011) 614–627.

[42] D. Komatitsch, J. P. Vilotte, The spectral element method: an effective tool to simulate the seismic response of 2D and 3D geological structures, Bull. Seism. Soc. Am. 88 (1998) 368–392.

[43] D. Komatitsch, C. Barnes, J. Tromp, Wave propagation near a fluid-solid interface: A spectral-element approach, Geophysics 65 (2) (2000) 623–631.

[44] Y. C. E. Chaljub, D. Komatitsch, J.-P. Vilotte, B. Valette, G. Festa, Spectral element analysis in seismology, in: Advances in Wave Propagation in Heterogeneous Media, Vol. 48 of Advances in Geophysics Series, Elsevier, 2007, pp. 365–419.

[45] P. Cance, Y. Capdeville, Validity of the acoustic approximation for elastic waves in heterogeneous media, Geophysics 80 (4) (2015) 161–173.

[46] A. T. De Hoop, Representation theorems for the displacement in an elastic solid and their application to elastodynamic diffraction theory, Ph.D. thesis, TU Delft, Delft University of Technology (1958).

[47] Y. Masson, P. Cupillard, Y. Capdeville, B. Romanowicz, On the numerical implementation of time-reversal mirrors for tomographic imaging, Geophys. J. Int. 196 (3) (2014) 1580–1599.

[48] G. Festa, J.-P. Vilotte, The newmark scheme as velocity-stress time-staggering: an efficient pml implementation for spectral element simulations of elastodynamics, Geophys. J. Int. 161 (3) (2005) 789–812.

[49] D. Givoli, Time reversal as a computational tool in acoustics and elastodynamics, J. Comput. Acoust. 22 (03) (2014) 1430001.

[50] Y. Cheng, C. Zhou, Q. Wei, D. Wu, X. Liu, Acoustic subwavelength imaging of subsurface objects with acoustic resonant metalens, Appl. Phys. Lett. 103 (22) (2013) 224104.

[51] F. P. Mechel, Formulas of acoustics, Springer Science & Business Media, 2013.

[52] N. Kaina, F. Lemoult, M. Fink, G. Lerosey, Negative refractive index and acoustic superlens from multiple scattering in single negative metamaterials, Nature 525 (7567) (2015) 77–81.

[53] F. Lemoult, N. Kaina, M. Fink, G. Lerosey, Wave propagation control at the deep subwavelength scale in metamaterials, Nat. Phys. 9 (1) (2013) 55–60.

[54] Y. Capdeville, L. Guillot, J. J. Marigo, 1-D non periodic homogenization for the wave equation, Geophys. J. Int. 181 (2010) 897–910.

[55] L. Guillot, Y. Capdeville, J. J. Marigo, 2-D non periodic homogenization for the SH wave equation, Geophys. J. Int. 182 (2010) 1438–1454.

[56] Y. Capdeville, L. Guillot, J. J. Marigo, 2D nonperiodic homogenization to upscale elastic media for P-SV waves, Geophys. J. Int. 182 (2010) 903–922.

[57] Y. Capdeville, M. Zhao, P. Cupillard, Fast fourier homogenization for elastic wave propagation in complex media, Wave Motion 54 (2015) 170–186.

[58] E. Sanchez-Palencia, Non homogeneous media and vibration theory, no. 127 in Lecture Notes in Physics, Springer, Berlin, 1980.

[59] G. Burgos, Y. Capdeville, L. Guillot, Homogenized moment tensor and the effect of near-field heterogeneities on nonisotropic radiation in nuclear explosions, J. Geophys. Res. (2016) In press.

[60] H. Ammari, E. Bonnetier, Y. Capdeboscq, Enhanced resolution in structured media, SIAM Journal on Applied Mathematics 70 (5) (2009) 1428–1452.

[61] C. Gomez, Time-reversal superresolution in random waveguides, Multiscale Modeling & Simulation 7 (3) (2009) 1348–1386.

[62] P. Letourneau, Fast algorithms and imaging in strongly-scattering media, Ph.D. thesis, Stanford University (2013).

[63] H. Ammari, H. Zhang, A mathematical theory of super-resolution by using a system of sub-wavelength helmholtz resonators, Commun. Math. Phys. 337 (1) (2015) 379–428.

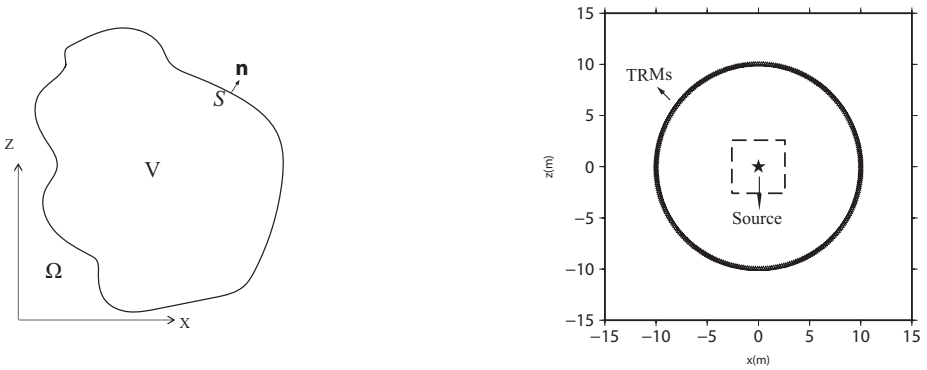

(a) (b)

Figure 1: (a): the infinite domain $\mathbf{\Omega}$, the contour S enclosing the domain $\mathbf{V}$ and its outward normal $\mathbf{n}$. (b): numerical experiment set up where the TRM is the "time reversal mirror".

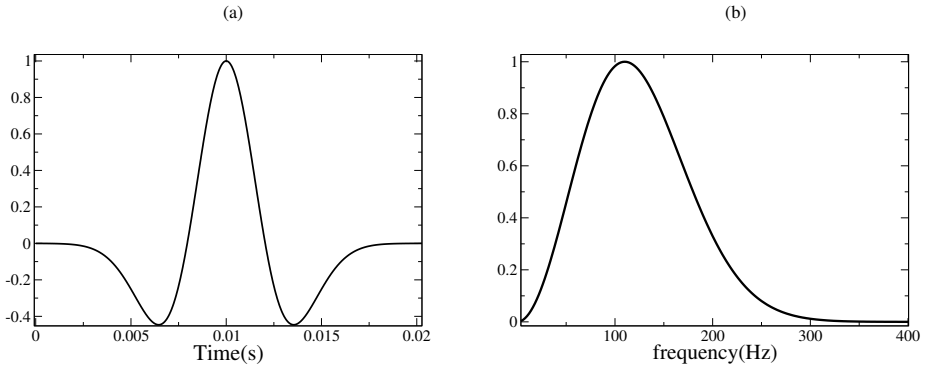

Figure 2: (a): Ricker source time wavelet with $t_0 = 0.01s$ and $f_0 = 100Hz$; (b): its amplitude spectrum.

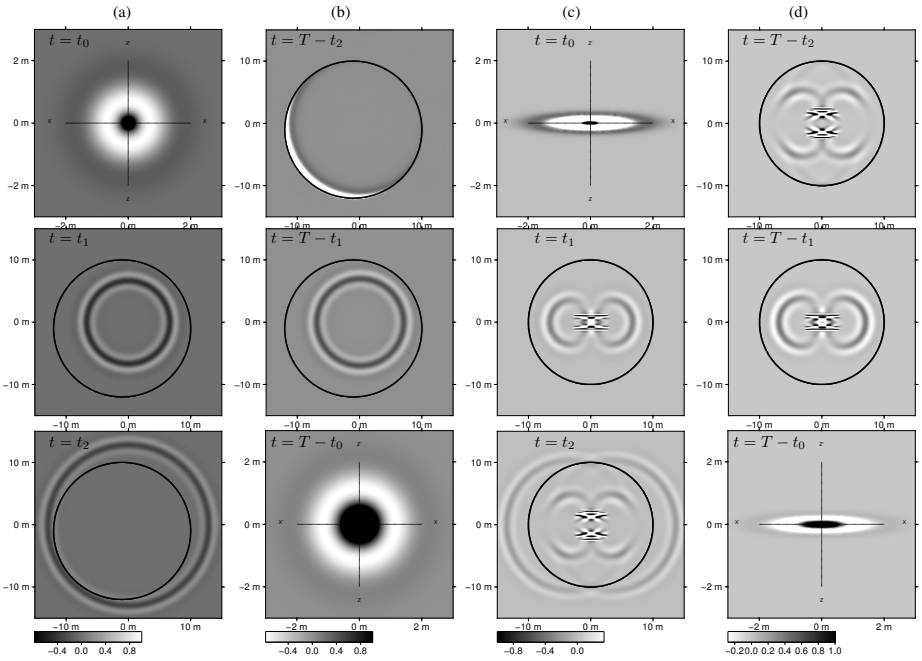

Figure 3: Pressure field snapshots at different time steps for the forward modeling step in a homogeneous medium (a), for the corresponding backward step (b), for the forward step in the anisotropic medium (c) and for the corresponding backward step (d). $t = t_0$ is the source origin time for the forward modeling sequences (a) and (c). $t = T - t_0$ corresponds to the focusing time for the backward modeling sequences (b) and (d). For the homogeneous case $t_0 = 0.02s$, $t_1 = 0.04s$, $t_2 = 0.058s$ and $T = 0.1s$. For the anisotropy case, $t_0 = 0.01s$, $t_1 = 0.03s$, $t_2 = 0.05s$ and $T = 1.0s$. Note that panels don't have all the same spatial scale. The TRM circle has deliberately not been centered on the source for the left plots (a) and (b): it shows that the position of the TRM with respect to the source is irrelevant to its capacity to focus the wavefield back to the source location.

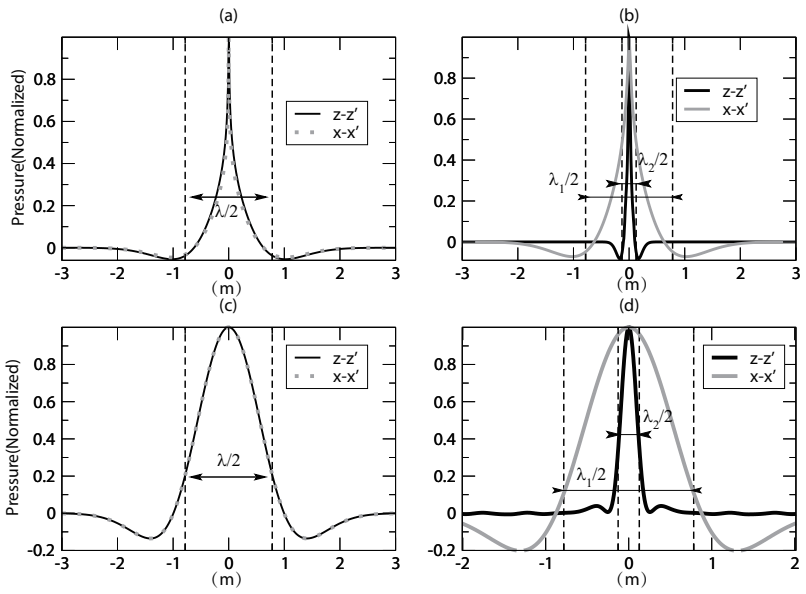

Figure 4: Pressure field cross-sections along the horizontal ($x - x'$) and vertical ($z - z'$) axis for the forward modeling step at the origin time $t = t_0$ (a) and for the backward step at the focusing time $t = T - t_0$ (c), both computed in the homogeneous medium. In (b) and (d) are presented the same cross-sections but computed in the anisotropic medium. λ is the dominant wavelength in the homogeneous medium. λ_1 and λ_2 are the two dominant wavelengths in the anisotropic medium.

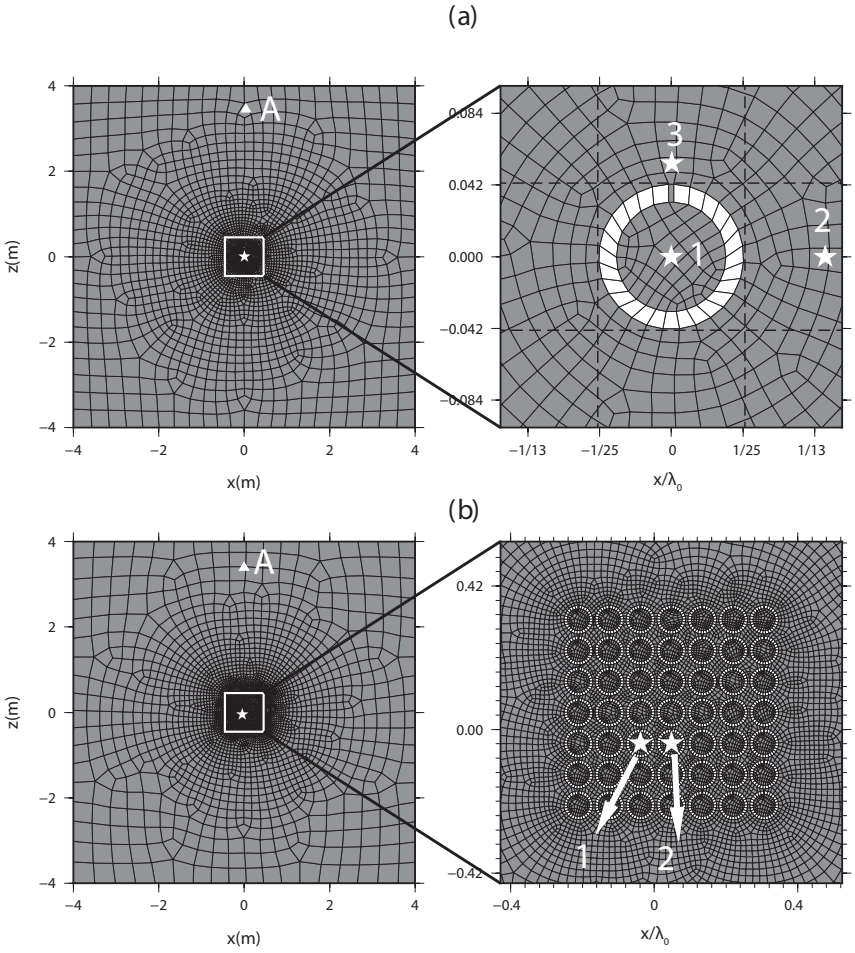

Figure 5: Spectral element mesh of the medium in the one ring case (a) and in the 7×7 rings case (b). "A" is the position of one receiver located on the TRM. The stars show the source 1, 2 and 3 locations.

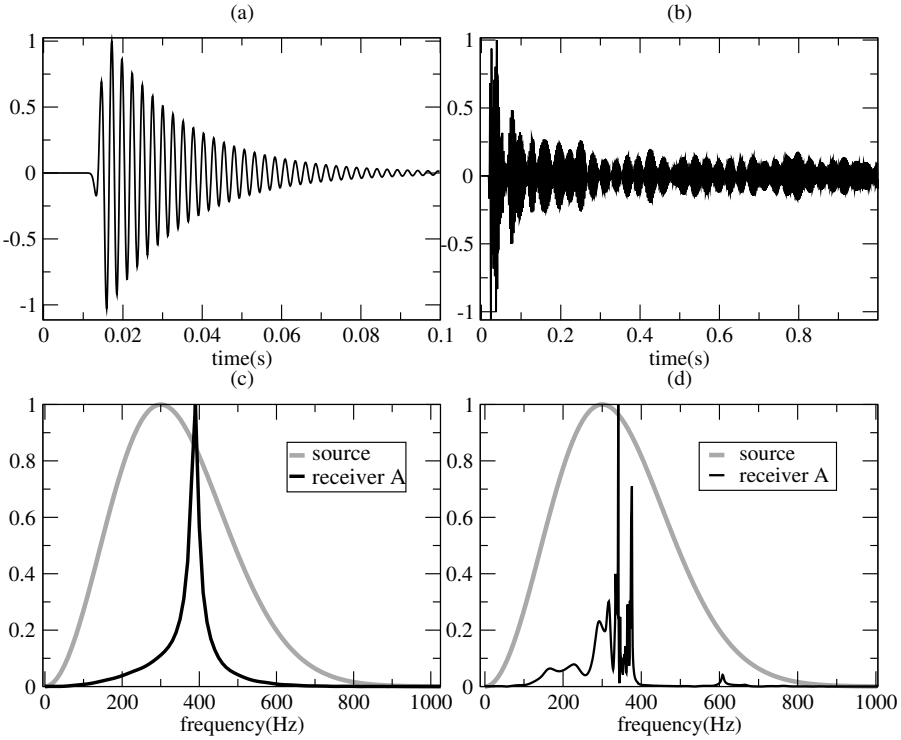

Figure 6: The time domain pressure signal recorded at receiver A (see Fig. 5) for the one ring (a) and multiple rings (b) cases; (c) and (d), are the corresponding amplitude spectra together with source wavelet amplitude spectra for comparison .

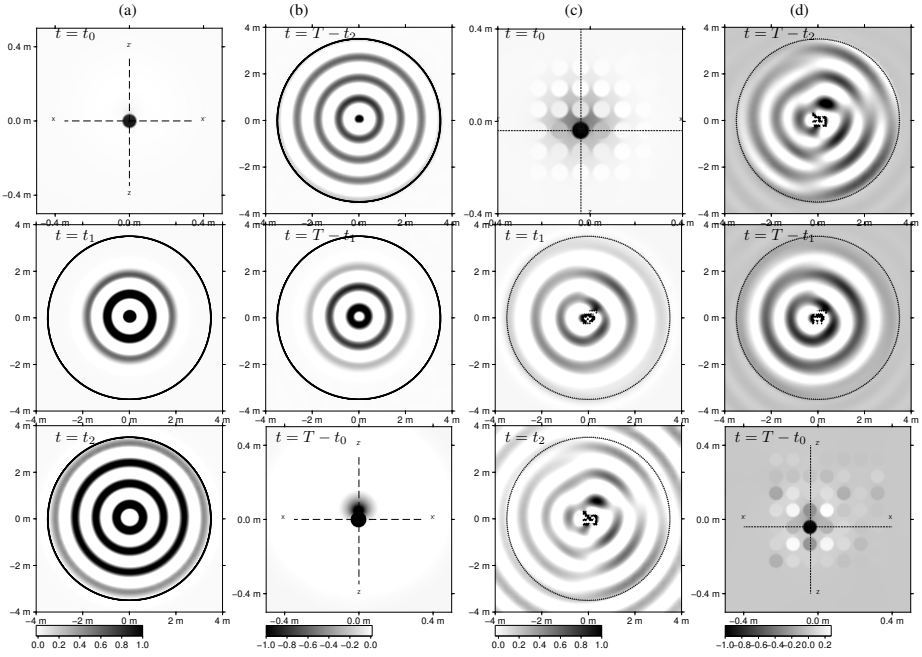

Figure 7: Pressure field snapshots, computed for a source central frequency $f_0 = 300Hz$, at different time steps for the forward modeling step in the one ring case (a), for the corresponding backward step (b), for the forward step in the multiple rings case (c) and for the corresponding backward step (d). $t = t_0$ is the source origin time for the forward modeling sequences (a) and (c). $t = T - t_0$ corresponds to the focusing time for the backward modeling sequences (b) and (d). For the one-ring case, $t_0 = 0.01s$, $t_1 = 0.015s$, $t_2 = 0.019s$ and $T = 0.1s$. For the multiple rings case, $t_0 = 0.01s$, $t_1 = 0.02s$, $t_2 = 0.03s$ and $T = 0.5s$. Note that panels don't have all the same spatial scale.

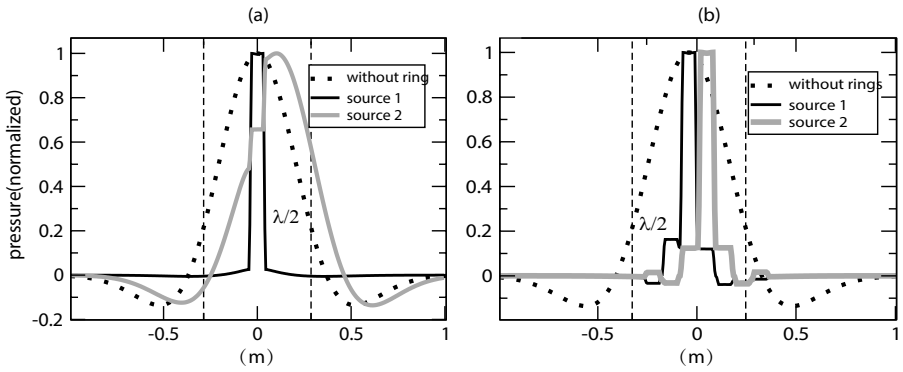

Figure 8: Pressure field cross-sections along the horizontal $(x - x')$ axis for backward step at the focusing time $t = T - t_0$ computed in the one ring medium (a). Three different source locations (see Fig. 5a): source 1 is in the ring and source 2 is at the rightside of the ring, source 3 is above the exit of the ring, the distance between each two sources is about $\lambda/13$, where λ is the dominant wavelength in the background air. In (b) are presented the same cross-sections but computed in the multiple rings medium. Two source locations in two different rings are used (see Fig. 5b). The focusing spot obtained in the background air ("without ring" line) is also displayed for comparison.

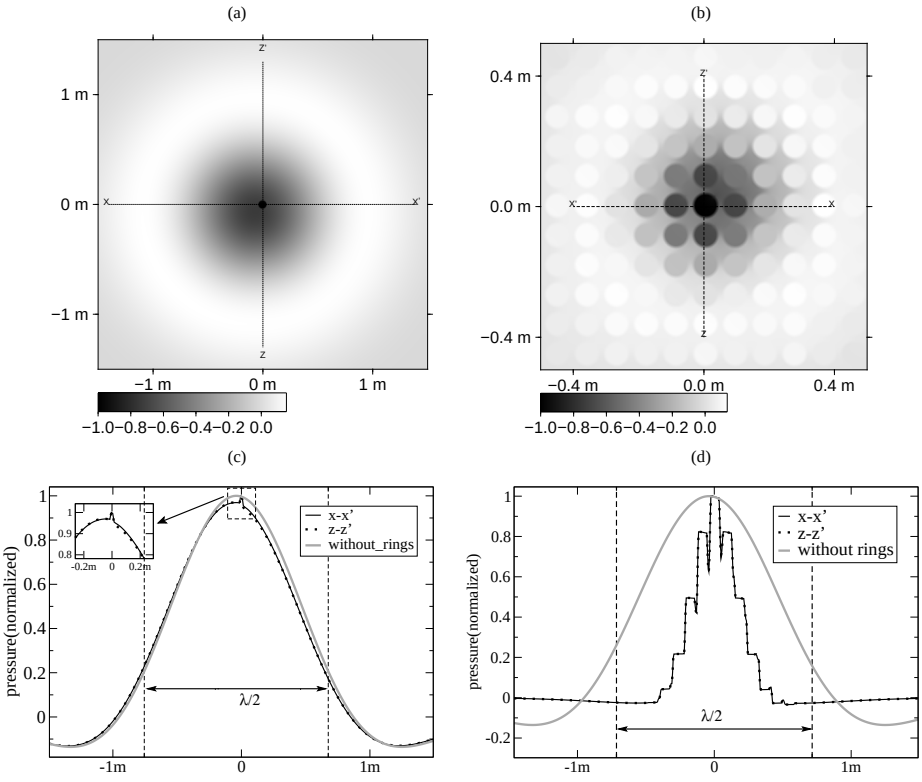

Figure 9: Pressure field snapshots at the focusing time for a source central frequency $f_0 = 100Hz$ in the single ring medium (a) and in the multiple rings medium (b). The two bottom panels (c) and (d) show cross-section in the above pressure field, along vertical and horizontal axis. The focusing spot obtained in the background air ("without ring" line) is also displayed for comparison.

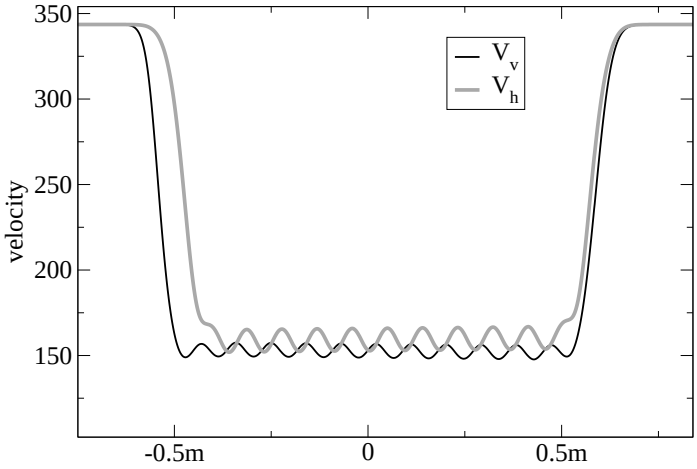

Figure 10: Cross-section along the x axis of the two effective velocities $V_h^* = \sqrt{\kappa^* L_{11}^*}$ and $V_v^* = \sqrt{\kappa^* L_{22}^*}$, computed with the non-periodic homogenization, through the mutiple rings medium a minimum wavelength of 0.3 m. The observed slight effective anisotropy is a common effect of upscaling.